Ultrafast photo-induced enhancement of electron-phonon coupling in metal-halide perovskites

Mingcong Wang,[1,] Yajun Gao,[1] Kai Wang,[1] Stefaan De Wolf,[1] Frédéric Laquai[1,*].*

[1]King Abdullah University of Science and Technology (KAUST), KAUST Solar Center (KSC), Physical Sciences and Engineering Division (PSE), Materials Science and Engineering Program (MSE), Thuwal 23955-6900, Kingdom of Saudi Arabia

Corresponding Author

*Mingcong Wang: mingcong.wang@kaust.edu.sa;

*Frédéric Laquai: frederic.laquai@kaust.edu.sa

ABSTRACT: In metal-halide perovskites (MHPs), the nature of organic cations affects both, the perovskite's structure and its optoelectronic properties. Using ultrafast pump-probe spectroscopy, we demonstrate that in state-of-the-art mixed-cation MHPs ultrafast photo-induced bandgap narrowing occurs, and linearly depends on the excited carrier density in the range from 10^{16} cm^{-3} to above 10^{18} cm^{-3}. Furthermore, time-domain terahertz (td-THz) photoconductivity measurements reveal that the majority of carriers are localized and that the localization increases with the carrier density. Both observations, the bandgap narrowing and carrier localization, can be rationalized by ultrafast (sub-2ps) photo-induced enhancement of electron-phonon coupling, originating from dynamic disorder, as clearly evidenced by the presence of a Debye relaxation component in the

terahertz photoconductivity spectra. The observation of photo-induced enhancement of electron-phonon coupling and dynamic disorder not only provides specific insight into the polaron-strain distribution of excited states in MHPs, but also adds to the development of a concise picture of the ultrafast physics of this important class of semiconductors.

Introduction

Understanding the excited carrier (photo) physics of metal-halide perovskite semiconductors is essential to unleash their optimum performance in optoelectronic applications, for instance, in light-emitting diodes and solar cells. In metal-halide perovskites Wannier-type excitons are the primary photo-generated states, since the small reduced electron mass (~0.1-0.15 m_e) [1-2] and high optical relative permittivity (ε_{opt}~4-6.5) [3] yield a Bohr radius larger than the perovskite's lattice constant. Based on the Wannier-exciton approximation, the exciton binding energy (R_b) can be estimated to ~54 meV when using $\varepsilon_{opt} = 5$ in the hydrogen model[2]. However, R_b~5-15 meV was determined based on temperature-dependent measurements of the absorption spectra of the classic $CH_3NH_3PbI_3$ (MAPbI) perovskite, analyzed in the framework of Elliot theory [4-6]. Such small R_b can be explained when considering strong electron-phonon coupling, resulting from the perovskites' polar ionic crystal structure, which screens efficiently the electron-hole mutual attraction potential [7-8]. In fact, excitons are barely observed in metal halide perovskites at room temperature (where the thermal energy k_BT is ~25 meV) due to efficient thermally-assisted dissociation. Consequently, free carriers are generated by photoexcitation, indicated by the quadratic carrier-density dependence of spontaneous photon emission [9].

Nevertheless, the excited carriers are not entirely free in perovskite semiconductor films. First, the carrier's effective mobility is reduced by static disorder, caused by imperfections and thin-film inhomogeneities[10,11]. Second, the perovskite's ionic crystal lattice is soft. As a result, lattice distortions follow the motion of carriers, leading to the formation of quasiparticles known as polarons [12]. Furthermore, the energetic barrier for rotation of the organic cations present in the perovskite lattice is as small as ~20 meV [13]. Consequently, the organic cations can rotate around their lattice positions at room temperature, thereby increasing dynamic disorder [14]. Therefore, carriers can be scattered and trapped in localized states induced by static disorder, lattice distortions, and/or dynamic disorder [15]. The intimate relation between carrier localization and dynamic disorder has been revealed by density functional theory (DFT) [15-20]. It has been shown that dynamic disorder contributes to the discrepancy between the theoretically-predicted and experimentally-observed temperature dependence of polaron mobility [14-15]. The latest interpretation is that carrier localization is induced by dynamic disorder, but stabilized by lattice distortion [20], or in other words, dynamic disorder is linked to polaron formation [18-19], as also observed experimentally [21-22]. Since dynamic disorder scales with temperature, it enhances electron-phonon coupling and increases carrier localization at higher temperatures [23], and thereby affects the polaron formation in the perovskite bulk [20]. However, the precise effect of dynamic disorder on electron-phonon coupling of excited states has remained elusive.

In this work, we employed transient absorption (TA) pump-probe spectroscopy to study electron-phonon coupling in an archetypical triple-cation perovskite film, namely $FA_{0.81}MA_{0.14}Cs_{0.05}PbI_{2.55}Br_{0.45}$ (FAMACs). This perovskite composition delivers a power conversion efficiency (PCE) higher than 20% in conjunction with excellent photostability in perovskite solar cells (PSCs) [24-25]. Carrier density-dependent TA spectra were measured at room

temperature across carrier density ranges comparable to those observed at 1-sun illumination and above, precisely in the range from N~3.6×10^{16} cm^{-3} to N~5.8×10^{18} cm^{-3}. We developed a model to analyze the high-energy tail of the TA spectra and revealed photo-induced bandgap renormalization (BGR). Our results demonstrate that BGR concludes in ~2 ps and, unexpectedly, exhibits a linear dependence on the photo-excited carrier density. This linear dependence cannot be rationalized by carrier-carrier interactions, suggesting that electron-phonon coupling is its origin [26]. More precisely, for polaron formation, this anomalous BGR can only be rationalized by considering photo-enhanced electron-phonon coupling. We evidenced the presence of photo-enhanced electron-phonon coupling by time-domain terahertz (tdTHz) spectroscopy. Specifically, we find that the fluence-dependent THz photoconductivity spectra can be described by a combination of the classical Drude model and the Debye relaxation model. The Debye relaxation component in the THz photoconductivity increases with carrier density, indicating an increase of the static-dielectric response, and thus enhancement of electron-phonon coupling at high carrier densities. The stabilization of this enhancement appears to be ultrafast, because the THz photoconductivity reaches its maximum in 2 ps. Since Debye relaxation is characteristic for dynamic disorder [27], we ascribe the origin of the photo-enhanced electron-phonon coupling to dynamic disorder. The fraction of Drude-type carriers compared to the total number of photo-generated carriers decreases from ~10% to 5% as the carrier density increases from N~1×10^{17} cm^{-3} to N~5×10^{18} cm^{-3}, indicating that most carriers remain localized. This localization is even enhanced at high carrier densities, a consequence of increased dynamic disorder[15,20]. Due to the low fraction of Drude-type carriers, the effective carrier mobility is about an order smaller than the expected Drude-type carrier mobility, indicating that one has to account for fraction of localized carriers, when determining effective carrier mobilities. Finally, yet importantly, we relate

the effective carrier density to the electron-phonon coupling constant and extract the photo-enhanced fraction, which is in excellent agreement with the value predicted by linear BGR.

Our findings imply that dynamic disorder plays a major role in the physics of excited states in perovskites. More precisely, at low-fluence, dynamic disorder increases electron-phonon coupling and carrier localization on ultrafast timescales (<2 ps), providing polaron strain gradients that can drive halide segregation [28]. For carrier densities above a critical value, N_C~5.3×10^{18} cm^{-3}, the polaron strain gradients are gradually released due to spatial overlap of neighboring polarons, an effect that can be exploited to cure light-induced halide segregation [28]. Since the effective carrier mobility decreases with carrier density, the carrier diffusion length decreases at high carrier densities. Consequently, the tradeoff between these two effects has to be considered when designing high performance perovskite optoelectronic devices.

Transient absorption spectra – Analysis of the high-energy tail of the photobleach

FAMAC films (thickness *d*~300 nm) were prepared by solution-processing of FAMAC solutions on spectroscopic-grade quartz substrates (see SI). Figure 1a shows the steady-state ground-state absorption spectrum, analyzed in the framework of the Elliott model, assuming the absorption (coefficient) consists of a linear combination of excitonic absorption (α_X) and absorption of continuum states (α_C) as reported earlier [4-6, 8, 29]. According to the Elliott theory, α_C is enhanced by a factor ξ due to Coulomb attraction between electrons and holes [6]:

$$\xi(R_{b0}, x) = \frac{2\pi\sqrt{R_{b0}/x}}{1 - \exp\left(-2\pi\sqrt{R_{b0}/x}\right)} \quad (1)$$

where R_{b0} is the exciton binding energy, and x=E-E_g, where E_g is the band gap. ξ approaches unity when $R_{b0} \rightarrow 0$, which implies the Coulomb enhancement of α_C does not exist any longer once excitons are fully screened. Using ξ, the Elliott formula can be expressed by [6]:

$$\alpha(E) = A\frac{4\pi R_{b0}^{3/2}}{E}\delta(x + R_{b0}) + A\frac{\xi(R_{b0}, x)}{E}\sqrt{x} \quad (2)$$

where A is a fitting parameter related to the transfer matrix elements [29], δ is the Dirac delta function, $\sqrt{x}$ is the normalized density of states in the conduction band assuming a parabolic shape (valid below ~1.82 eV in our sample). The first term accounts for α_X, while the second term accounts for $\xi\alpha_C$. To describe the room-temperature absorption spectra, a hyperbolic-secant broadening function accounting for thermal and inhomogeneous broadening was convoluted with Eqn. 2 (see SI), yielding R_{b0} ~ 7.4 meV and E_g ~ 1.67 eV (Fig. 1a). The decomposed α_X and $\xi\alpha_C$ are plotted in Figure 1a alongside α_C. Clearly, the high-energy part of the absorption spectrum is very sensitive to ξ, the Coulomb screening.

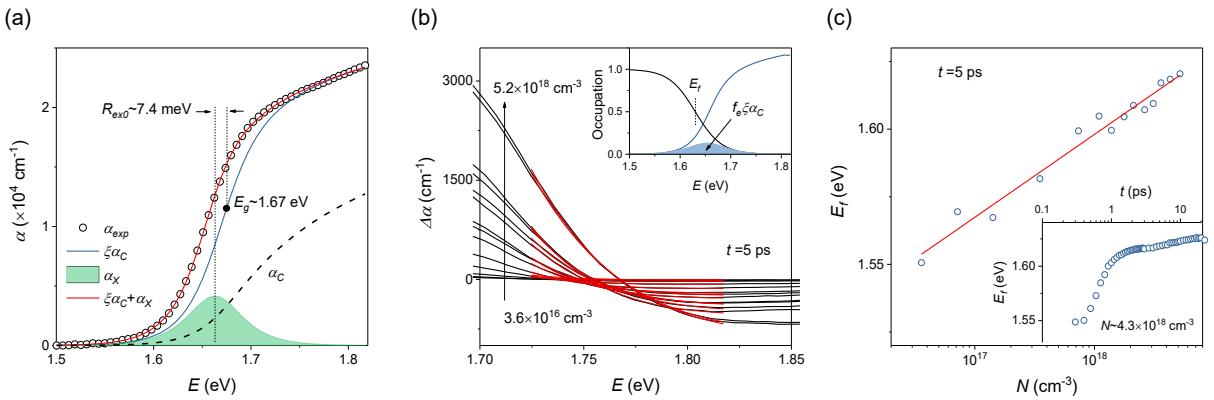

Figure 1. Fit of the thin film ground-state absorption spectra and of the high-energy part of the TA spectra to the Elliott model. (a) Elliott model fit to the ground-state absorption spectra of thin films. The dashed line exemplifies the continuum absorption, if excitons are fully screened (ξ=1). **(b)** High energy part of TA spectra recorded at 5 ps delay for carrier densities varying from 3.6×10^{18} to 5.2×10^{18} cm^{-3}. The pump wavelength was 475 nm (~2.61 eV). Red lines are fits of the TA spectra between 1.72 eV and 1.82 eV to the Elliott model. Inset: a schematic of the occupational probability in the conduction band. **(c)** Plot of the quasi-Fermi level energy (E_f)

against the carrier density. The red solid line is a linear fit to E_f as a function of log(N). Inset: time-dependent E_f for a carrier density of ~4.3 $\times 10^{18}$ cm^{-3}.

Next, we focus on the high-energy part of the TA spectra to explore the photo-induced BGR and underlying many-body effects (Fig. 1b). When analyzing the high-energy part of the spectra, we can safely neglect photo-induced broadening. For x larger than the width of the broadening function, the high-energy tails can be described by (see SI):

$$\Delta\alpha(E) \cong A\frac{\xi\left(R_b, x+\Delta E_{bgr}\right)}{E}\sqrt{x+\Delta E_{bgr}}(1-f_e)^2 - A\frac{\xi(R_{b0}, x)}{E}\sqrt{x} \quad (3)$$

where R_b and ΔE_{bgr} are the screened exciton binding energy and the photo-induced BGR due to many-body effects, respectively. Here a positive ΔE_{bgr} represents bandgap narrowing. f_e=1/[1+$e^{(E-E_f)/k_BT_e}$] is the Fermi-Dirac distribution function accounting for the occupation probability of electrons in the conduction band (inset in Fig. 1b), where E_f is the quasi-Fermi level, k_B is the Boltzmann constant, and T_e is the absolute electron temperature. Since the effective mass of holes is similar to that of electrons [30], we assume that the occupation probability of holes in the valence band is symmetric to that of electrons in the conduction band. Compared to fits of the entire TA bleach region [31-32], Eqn. 3 only uses four fitting parameters, namely R_b, ΔE_{bgr}, E_f and T_e, owing to the intrinsic independence of the broadening function. Using the fitting results of the ground-state absorption spectrum (see Fig. S1, A=59451, R_{b0}=7.4 meV and E_g =1.67 eV), the high-energy tails (E~1.72 eV-1.82 eV) can be described very well by Eqn. 3 (Fig.1b). Here, R_b=R_{b0} was used in the fitting, since even a small reduction in R_b resulted in poor fits.

The time-dependent E_f for N~4.3×10^{18} cm^{-3} exhibits a fast picosecond rise followed by a slow rise in the range of tens of picoseconds (inset in Fig. 1c). This is related to hot-carrier cooling limited by the phonon bottleneck. If the value of E_f is smaller than E_g, then the electron density can be approximated by [6, 31]:

$$N \cong 2\left(\frac{m^* k_B T_e}{2\pi\hbar}\right)^{3/2} \exp\left(\frac{E_f - E_g}{k_B T_e}\right) \quad (4)$$

where m^* is the effective electron mass and the other parameters have been defined above or have their usual meaning. E_f mainly depends on T_e at early times when N is constant, thus its time-dependent evolution mimics the effect of hot-carrier cooling. The reason for the cooling bottleneck has been summarized recently, [33] and it is not the focus of this work. Eqn. 4 also shows that E_f is linear in log(N) once hot-carrier cooling has concluded (Fig. 1c).

Dependence of BGR on photo-excited carrier density

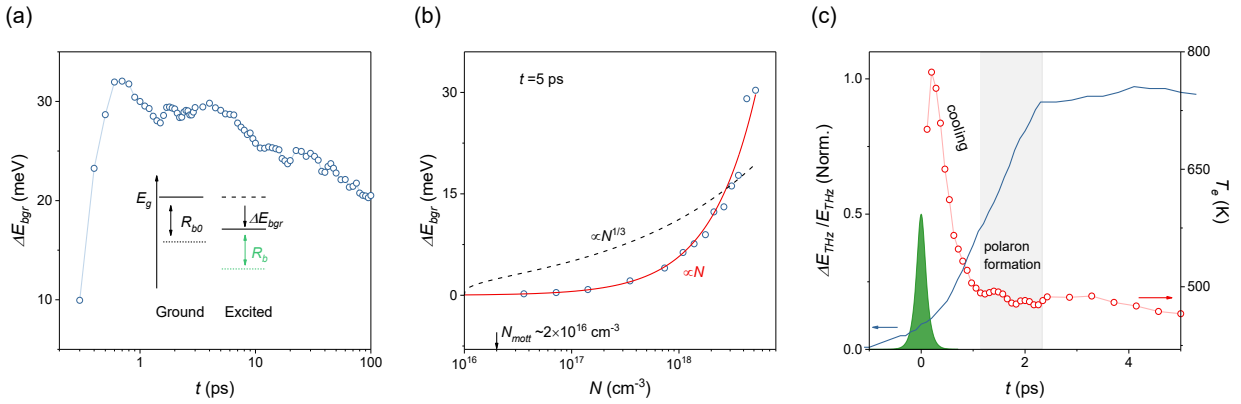

Figure 2. Photo-induced bandgap renormalization (BGR) in perovskites. (a) Time-dependent BGR for a carrier density of ~4.3 ×10^{18} cm^{-3}. Inset: a schematic of the bandgap narrowing due to BGR. The exciton binding energy after BGR is indicated by a green double-headed arrow. **(b)** BGR against carrier density. The dashed line is a power law fit with $\Delta E_{bgr} \propto N^{1/3}$. The red solid line is a fit with $\Delta E_{bgr} \propto N$. Black arrow: the Mott density estimated from the exciton band energy. **(c)** Left axis: Normalized terahertz kinetics for a carrier density of ~4.3 ×10^{18} cm^{-3}. The green area represents the correlation (pulse width ~176 fs) of pump and probe laser pulses. Right axis: time evolution of electron temperature (T_e) after photoexcitation. T_e reaches its maximum soon after the instrument response (~352 fs), yet the terahertz kinetics indicate a maximum at ~2 ps. The rise of the terahertz kinetics observed after hot-carrier cooling has concluded is an evidence of polaron formation (shaded area).

For N~4.3×10^{18} cm^{-3}, ΔE_{bgr} assumes a plateau between ~2-5 ps after reaching the maximum (Fig. 2a), indicating photo-induced BGR is concluded in ~2 ps. The subsequent decrease of ΔE_{bgr}

after ~5 ps is caused by the onset of carrier recombination. The stabilized ΔE_{bgr} is ~29 meV, similar to the value extracted from MAPbI films [31]. Since our data can only be fitted with $R_b=R_{b0}$, the nonzero ΔE_{bgr} implies that the excitonic level is red-shifted by ΔE_{bgr} (schematic in Fig. 2a). Such phenomenon cannot be explained by carrier-carrier interactions, which should leave the excitonic level virtually unchanged, because the photo-induced BGR and screening occur at the same time [34]. We note that the formation of bi-excitons may cause a large redshift of the excitonic level [35]. However, this is not observed here. Hence, we conclude that ΔE_{bgr} must be caused by electron-phonon interactions [26].

It is noteworthy that $R_b=R_{b0}$ does not imply the absence of photo-induced screening, rather the photo-induced screening occurs on longer time scales, which do not affect R_b [14]. This time scale can be estimated by $t_{scr}>R_{b0}/h$, where h is the Planck constant, yielding $t_{scr}>554$ fs. Despite t_{scr} larger than the time resolution of our TA spectroscopy setup (~176 fs), stabilized excitons are hardly detected due to very efficient thermal dissociation. In the framework of the hydrogen model, the effective exciton dielectric response (ε_X) at the ground state can be evaluated by: $R_{b0}=13.6m_r/(m_e\varepsilon_X^2)$ eV, where 13.6 is the Rydberg constant and m_r is the reduced electron mass. Here we obtain ε_X ~14.85 when using $m_r=0.12\ m_e$ (ref. 1-2). According to the Mott transition criterion of $a_B/\lambda_D=1.19$, [36] where $a_B=0.0592m_e\varepsilon_X/m_r$ is the effective Bohr radius of the exciton and $\lambda_D=[\varepsilon_X E_T/(8\pi e^2 N)]^{1/2}$ is the Debye screening length, using the thermal energy E_T ~25 meV at room temperature, the estimated Mott density in our sample is $N_{Mott}\sim 2\times10^{16}$ cm^{-3} (Fig. 2b), indicating, hot excitons are separated instantaneously by phonon scattering if $N>2\times10^{16}$ cm^{-3}.

The stabilized value of ΔE_{bgr} plotted versus the carrier density is shown in Figure 2b; likewise, the dependence cannot be explained by carrier-carrier interactions. In fact, in a doped semiconductor where carrier-carrier interactions are dominant, BGR should follow a power law

dependence on the carrier density according to: $\Delta E_{bgr} \propto N^k$, where k~1/3, when electron-defect scattering is not significant [37-38]. However, Figure 2b shows k~1 in our sample, which cannot be explained by carrier-carrier interactions. The same results are found in other mixed-cation perovskites (see Fig. S2). The k=1 dependence can also result from electron-phonon interactions. Perovskites are polar materials and their static-dielectric responses (ε_s) are much larger than the optical ones (ε_{opt}) [3, 14], resulting in pronounced Fröhlich electron-phonon coupling according to:

$$a_{ep} = \frac{1}{137}\sqrt{\frac{m^* c^2}{2\Omega_{LO}}}\left(\frac{1}{\varepsilon_{opt}} - \frac{1}{\varepsilon_s}\right) \quad (5)$$

where 1/137 is the fine structure constant, c is the speed of light, and Ω_{LO} is the effective beating energy of longitudinal optical (LO) phonons. a_{ep}~1.8-3.2 is obtained for the ground state when using ε_{opt}=4-6.5 (ref. 3), ε_s=35 (ref. 3), Ω_{LO}/h~3.7 THz (ref. 36), and m^*=0.23 m_e (ref. 27), yielding a bandgap narrowing of $E_{pol} \sim a_{ep}\Omega_{LO}$ = 27.3-48.3 meV, induced by the electron polaron formation [40]. The narrowing is expected to double when hole polarons are also involved [40]. While we have no clear evidence of polaron formation, indirect evidence is found when comparing the hot-carrier cooling with the rise of the time-resolved terahertz signal. Figure 2c shows that the terahertz photoconductivity has reached only half of its maximum when hot-carrier cooling has concluded, indicating electron-phonon interactions are the main reason for the rise in the first 1-2 ps. This phenomenon has been ascribed unambiguously to polaron formation in single-cation perovskites [41].

Generally, E_{pol} does not contribute to ΔE_{bgr}, because it is contained in the ground-state absorption spectrum from which E_g is extracted (Fig. 1a). However, if a_{ep} is enhanced by photoexcitation, E_{pol} can contribute to ΔE_{bgr} according to:

$$\Delta E_{bgr} \sim 2\Delta a_{ep}\Omega_{LO} \quad (6)$$

This enhancement can be enabled by the presence of coupling between photon-induced dynamic disorder and the lattice distortion [21-22].

Photo-enhanced dielectric response

The photo-enhanced dielectric response was first revealed by electrical experiments [42-43], however, the conclusions have remained debated [44]. Here we provide further evidence based on tdTHz spectroscopy. Following the measurement of the tdTHz spectrum without prior photoexcitation (E_{THz}), the photo-induced tdTHz spectra (ΔE_{THz}) were recorded at 5 ps after photoexcitation (inset in Fig. 3a). The differential tdTHz spectra in the frequency domain ($\Delta E_{THz}/E_{THz}$) can be obtained by Fast Fourier Transformation (FFT), and subsequently the photo-induced change of the dielectric response ($\Delta\varepsilon_{THz}$) can be calculated by [45]:

$$\frac{\Delta E_{THz}}{E_{THz}} = -\frac{1}{\varepsilon_0 c(1+n_{sub})}\int_0^d \Delta\sigma(\omega,x)dx, \quad \Delta\varepsilon_{THz}(\omega) = \frac{i\Delta\sigma(\omega)}{\omega\varepsilon_0} \tag{7}$$

where ε_0 is the vacuum dielectric constant, c the speed of light, n_{sub}~2.13 the refractive index of the quartz substrate in the terahertz region, d is the sample thickness, $\Delta\sigma$ the photo-induced change of the photoconductivity, and ω is the angular frequency.

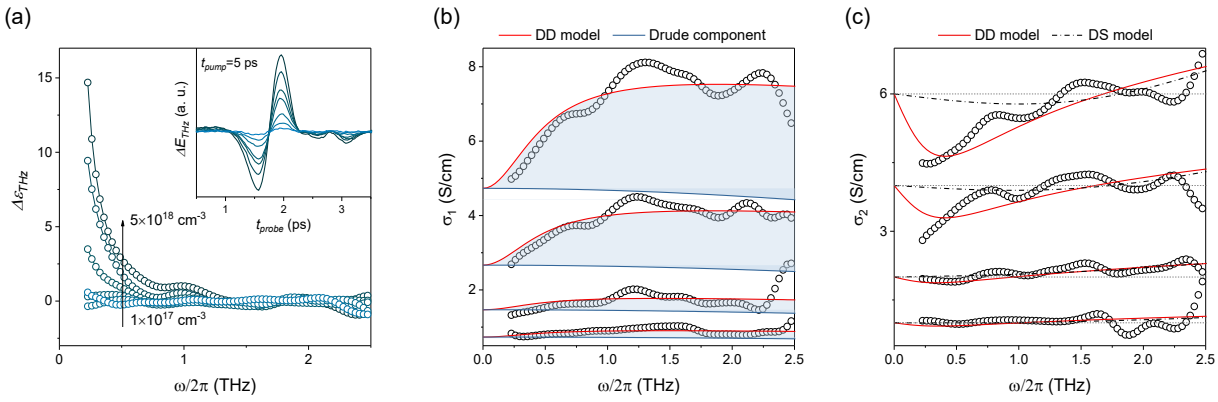

Figure 3. Photo-induced change of terahertz photoconductivity. (a) The photo-enhanced dielectric response in the terahertz region. Inset: the photo-induced change of the terahertz electric field recorded at 5 ps after photoexcitation for carrier densities varying from 1×10^{17} to 5×10^{18} cm^{-3}. The pump wavelength was 550 nm (~2.25 eV). **(b)** The real part of the photo-induced change of the terahertz photoconductivity. Red solid lines are fits using a combined Drude model and Debye relaxation model (DD model). Blue solid lines are the Drude components. Shaded areas represent the Debye relaxation components. **(c)** The imaginary part of the photo-induced change of the terahertz photoconductivity (stacked for clarity, dashed lines are zero lines). Red solid lines are fits to the DD model, dash-dotted lines are fits to the Drude-Smith model (DS model).

Figure 3a shows the real part of $\Delta\varepsilon_{THz}$ increases with carrier density, especially at low frequencies. This behavior is similar to the dielectric model of Debye relaxation related to dynamic disorder [27]:

$$\varepsilon(\omega) = \varepsilon_{opt} + \frac{\varepsilon_s - \varepsilon_{opt}}{1 - i\omega\tau_r} \tag{8}$$

where ε_s is the static dielectric constant and τ_r is the Debye relaxation time. τ_r is related to the phonon activation energy (E_a) and the thermal energy by $\tau_r = \tau_0 * \exp(E_a/E_T)$ with constant τ_0. Since E_T is determined by the lattice temperature, which does not change significantly, τ_r can be considered constant in our experiments. Eqn. 8 implies that dynamic disorder contributes to $\Delta\varepsilon_{THz}$. More precisely, the photo-induced low energy polarizations give rise to the dielectric response.

Next, we turn to the complex photoconductivity change $\Delta\sigma$, which is shown frequently in THz works (Fig. 3b-3c). At low carrier densities, $\Delta\sigma_1$ (the real part of $\Delta\sigma$) is virtually frequency independent (Fig 3b) and $\Delta\sigma_2$ (the imaginary part of $\Delta\sigma$) is close to zero (Fig. 3c). These spectral signatures indicate, the photoconductivity is mediated by free charges that undergo high rate scattering events [46]. At high carrier densities, $\Delta\sigma_1$ drops at the low frequency side and $\Delta\sigma_2$ shows a zero-crossing. Such behavior has been explained in the framework of the Drude-Smith model (DS model) which involves carrier localization [10]:

$$\Delta\sigma(\omega) = \frac{e^2}{m^*}\frac{N_D\tau_{sc}}{1-i\omega\tau_{sc}}\left[1+\sum_{j=1}\frac{c_j}{(1-i\omega\tau_{sc})^j}\right] \quad (9)$$

where e is the unit charge of electron, N_D is the density of Drude carriers, τ_{sc} is the carrier's momentum scattering time. c_j is a parameter ($-1 \le c_j \le 0$) that accounts for photoconductivity renormalization caused by the j-th scattering event. Here, the scattering time for each scattering event is considered unchanged. c_j=-1 implies full back scattering (no conduction), while c_j=0 implies no backscattering (Drude conduction). A negative c_j shifts the Drude response to high frequency.

The DS model fits well at low carrier densities, however, it cannot describe $\Delta\sigma_2$ at high carrier densities (Fig. 3c), indicating localized carriers exhibit different scattering times due to dynamic disorder. Since $\Delta\sigma_2$ is directly related to the real part of $\Delta\varepsilon_{THz}$ (Eqn. 7), we combined the Drude model and Debye relaxation model (DD model) to describe our data:

$$\Delta\sigma(\omega) = \frac{e^2}{m^*}\frac{N_D\tau_{sc}}{1-i\omega\tau_{sc}} - \frac{i\varepsilon_0\omega\Delta\varepsilon_s}{1-i\omega\tau_r} \quad (10)$$

where $\Delta\varepsilon_s$ is the photo-induced change of the static dielectric response originated from dynamic disorder. The first term on the right side of the equation accounts for the Drude photoconductivity, the second term accounts for the photoconductivity resulting from dynamic disorder. $\Delta\sigma_1$ and $\Delta\sigma_2$ can be well fitted globally by the DD model (Fig. 3b-3c), with τ_{sc}~16.7 fs and τ_r ~343 fs. The shaded area in Figure 3b represents the photoconductivity originating from dynamic disorder, which tends to become zero at ω=0, indicating dynamic disorder does not support long range photoconductivity.

Discussion

The fraction of Drude carriers among all photo-generated carriers (N_D/N) is shown in Figure 4a (top panel), alongside the ratio of $\Delta\varepsilon_s/N$ (bottom panel in Fig. 4a). We find that N_D/N is only ~5%-10% depending on the carrier density, similar to the value determined for MAPbI films [10] and MAPbI single crystals [47]. $\Delta\varepsilon_s/N$ is almost constant, indicating a linear increase of $\Delta\varepsilon_s$ as carrier density increases. However, the uncertainty is significant at low carrier densities, because of the poor signal-to-noise ratio. To confirm that N_D/N and $\Delta\varepsilon_s/N$ do not change significantly at low carrier densities, the effective carrier mobility (μ_{eff}) was calculated by $\mu_{eff}=\mu N_D/N$ (Fig. 4b), where μ is the mobility of Drude carriers: $\mu=e\tau_{sc}/m^*\sim127.8$ cm^2/V/s. For comparison, the effective mobility was also directly calculated from the frequency-averaged $\Delta\sigma_1$ by $\mu_\sigma=\sigma_{avg}/Ne$ (Fig. 4b). We expected that $\mu_\sigma>>\mu_{eff}$ if $N_D/N \rightarrow 1$ at low carrier densities, however, Figure 4b shows μ_σ is only slightly larger than μ_{eff} for all carrier densities investigated, indicating that there is no significant change of N_D/N and $\Delta\varepsilon_s/N$ at carrier densities around $N\sim10^{17}$ cm^{-3}. The low value of N_D/N indicates μ_{eff} mainly originates from a small fraction of photo-generated carriers, consistent with the complicated localization nature in MHPs [15]. Our finding also suggests that μ_σ is a good approximation of μ_{eff} without the need to extract it from fits of the terahertz photoconductivity.

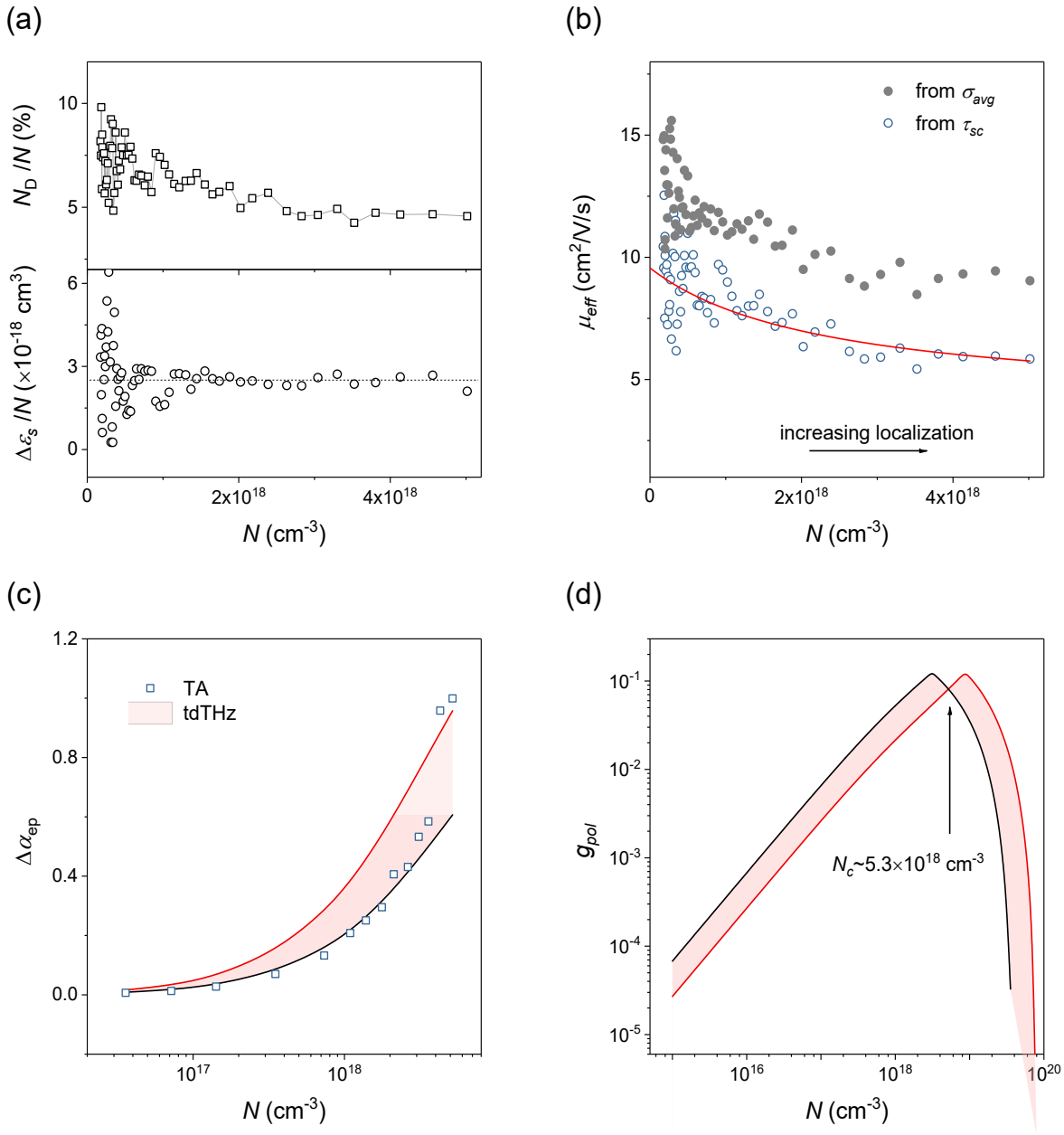

Figure 4. Carrier localization and effective carrier mobility in FAMACs films. (a) Top panel: The fraction of Drude carriers among all the photo-generated carriers. Bottom panel: Photo-induced change of static dielectric response, scaled by carrier density. The dashed line indicates $\Delta\varepsilon_s/N$=2.6×10^{-18} cm^3. **(b)** The effective carrier mobility obtained from the momentum scattering time (open circles) and the averaged photoconductivity (filled circles), respectively. The red solid line is a polaron mobility fit (Eqn. 11). **(c)** Photo-enhanced electron-phonon coupling (Δa_{ep}) obtained from TA spectra (open squares) and terahertz photoconductivity (pink area), respectively. Red solid lines are the upper limit and lower limit of Δa_{ep}, calculated by using different optical dielectric response (ε_{opt}). Red line: ε_{opt}=4. Black line: ε_{opt}=6.5. **(d)** Polaron strain gradients

evaluated by the volume ratio of polarons (see Eqn. 12 in the main text). The critical carrier density is indicated by black arrow. Red line: ε_{opt}=4. Black line: ε_{opt}=6.5.

Figure 4a shows N_D/N decreases with carrier density, indicating photo-enhanced carrier localization. The localized carriers likely form large polarons [15]. While 'polaronic excitons' may exist at room temperature, if the carrier density is sufficiently low (~10^{16} cm^{-3}) [48] or if the exciton binding energy is high (~200 meV) [49], stabilized excitons are unlikely to be present in our experiments (Fig. 2b). The enhanced carrier localization coincides with the increase of the shaded area in Figure 3b, confirming the intimate relation between carrier localization and dynamic disorder. Since a positive $\Delta\varepsilon_s$ will result in an increase of a_{ep} (Eqn. 5), in the weak-coupling regime, μ_{eff} can be related to Δa_{ep} by using the concept of polaron mobility [50]:

$$\mu_{eff} = \mu_0 \frac{a_{ep0}\left(1 + a_{ep0}/6\right)}{\left(a_{ep0} + \Delta a_{ep}\right)\left(1 + a_{ep0}/6 + \Delta a_{ep}/6\right)} \tag{11}$$

where μ_0 and a_{ep0} are the polaron mobility and Fröhlich electron-phonon coupling constant at $N\rightarrow 0$, respectively, and the term $1+a_{ep0}/6$ indicates the polaron mass is enhanced by a factor of ~$a_{ep}/6$ compared to the effective electron mass in the rigid lattice [50]. Combining Eqn. 5 and Eqn. 11, only three unknown parameters remain: Ω_{LO}, ε_{opt} and ε_s. For simplicity, we fit μ_{eff} by using $\Delta\varepsilon_s/N$=2.6×10^{-18}, Ω_{LO}/h=3.7 THz, and ε_{opt}~4-6.5 (Fig. 4b). The fitted ε_s is ~9-12.6, much smaller than the theoretically predicted value [3]. The discrepancy can arise from the uncertainty of Ω_{LO} and because electron-phonon coupling is primarily mediated by optical phonons [17, 51], which only contribute weakly to the static dielectric response [3].

With $\Delta\varepsilon_s$=2.6×$10^{-18}N$, Ω_{LO}/h=3.7 THz, ε_{opt}~4-6.5 and ε_s~9-12.6, Δa_{ep} is calculated and plotted in Figure 4c, in good agreement with the Δa_{ep} estimated from the TA experiments by Eqn. 6. As $\Delta\varepsilon_s$ was assigned entirely to optical phonons in the fit (Fig. 4b), the good agreement indicates

dynamic disorder is strongly coupled with lattice distortion, consistent with recent reports [21-22]. The coupling time is ultrafast (<2 ps, see rise in Fig. 2c) and related to the Debye relaxation time τ_r ~343 fs. Since Δa_{ep} is only determined by the carrier-density dependence of the dynamic disorder, its value is marginal at carrier densities below N~10^{17} cm^{-3} (Fig. 4c), indicating Δa_{ep} can be neglected for MHP solar cells that work under 1-sun illumination. However, Δa_{ep} exacerbates the polaron strain gradients and thereby the halide segregation [28]. Under high irradiance, Δa_{ep} reduces the carrier mobility and thus the carrier diffusion length.

Next, we use the volume ratio of polarons to evaluate the polaron strain gradient (g_{pol}). We note that, when two adjacent polarons merge, the polaron strain cancels in the overlapping part:

$$g_{pol} \sim \min\left[\frac{r_{pol}^3}{d_{pol}^3},\ \frac{\left(d_{pol}-2r_{pol}\right)^3}{d_{pol}^3}\right] \tag{12}$$

where r_{pol} is the Feynman polaron radius, [52] and d_{pol} is the distance between two neighboring polarons. The two can be approximated by:

$$r_{pol} = \hbar\sqrt{\frac{3v}{2m_e(v^2-w^2)\Omega_{LO}}}, \qquad d_{pol}^3 \approx \frac{1}{N} \tag{13}$$

where v=3+2a_{ep}/9 and w=3 are variable parameters in units of Ω_{LO}. [52] The calculated r_{pol} and d_{pol} are given in SFig. 3, and g_{pol} is plotted in Fig. 4d. When the carrier density increases, g_{pol} reaches its maximum at a critical carrier density of N_C~5.3×10^{18} cm^{-3}. When $N>N_C$, g_{pol} drops due to the spatial overlap of adjacent polarons. Therefore, high irradiance can be used to cure light-induced halide segregation and to alter the perovskite bandgap [28].

In conclusion, triple-cation-mixed MHP films (FAMACs) were investigated by TA spectroscopy and tdTHz spectroscopy. We developed a model to analyze the high-energy tails of the TA spectra, taking into account the exciton binding energy and the photo-induced BGR. We

demonstrate that the photo-induced BGR reveals ultrafast (<2 ps) photo-enhanced electron-phonon coupling, which has its origin in dynamic disorder, as evidenced by the Debye relaxation component observed in the terahertz photoconductivity spectra. Furthermore, we determined that photo-generated carriers are highly localized. Importantly, the effective carrier mobility can be approximated from the frequency-averaged terahertz photoconductivity measurements without further fits. Finally, we extracted the photo-enhanced electron-phonon coupling constant as a function of the carrier density, and we revealed ultrafast coupling (<2 ps) between dynamic disorder and the lattice distortion. Our findings provide insights into the ultrafast photophysics of perovskites, specifically the polaron strain distribution of excited states in perovskite devices and as a function of the photogenerated carrier density.

AUTHOR INFORMATION

The authors declare no competing financial interests.

AUTHOR CONTRIBUTIONS

M.W. performed the time-domain terahertz measurements and data analysis. He conceived and developed the theoretical model and wrote the initial draft of the paper. Y.G. performed the ground-state absorption and transient absorption measurements. K.W. prepared the perovskite thin film samples. S.D.W. and F.L. supervised the work and revised the manuscript. All authors contributed to refining the final version of the manuscript.

ACKNOWLEDGMENT

This publication is based upon work supported by the King Abdullah University of Science and Technology (KAUST) Office of Sponsored Research (OSR) under Award No: OSR-2018-CARF/CCF-3079.

REFERENCES

1. Miyata, A. *et al.* Direct measurement of the exciton binding energy and effective masses for charge carriers in organic–inorganic tri-halide perovskites. *Nature Phys* **11,** 582–587; 10.1038/nphys3357 (2015).
2. Tanaka, K. *et al.* Comparative study on the excitons in lead-halide-based perovskite-type crystals CH3NH3PbBr3 CH3NH3PbI3. *Solid State Communications* **127,** 619–623; 10.1016/S0038-1098(03)00566-0 (2003).
3. Wilson, J. N., Frost, J. M., Wallace, S. K. & Walsh, A. Dielectric and ferroic properties of metal halide perovskites. *APL Materials* **7,** 10901; 10.1063/1.5079633 (2019).
4. Even, J., Pedesseau, L. & Katan, C. Analysis of Multivalley and Multibandgap Absorption and Enhancement of Free Carriers Related to Exciton Screening in Hybrid Perovskites. *J. Phys. Chem. C* **118,** 11566–11572; 10.1021/jp503337a (2014).
5. Yamada, Y., Nakamura, T., Endo, M., Wakamiya, A. & Kanemitsu, Y. Photoelectronic responses in solution-processed perovskite CH3NH3PbI3 solar cells studied by photoluminescence and photoabsorption spectroscopy. *IEEE J. Photovolt.* **5**, 401–405; 10.1109/JPHOTOV.2014.2364115 (2015).
6. Davies, C. L. *et al.* Bimolecular recombination in methylammonium lead triiodide perovskite is an inverse absorption process. *Nature communications* **9,** 293; 10.1038/s41467-017-02670-2 (2018).
7. Menéndez-Proupin, E., Beltrán Ríos, C. L. & Wahnón, P. Nonhydrogenic exciton spectrum in perovskite CH 3 NH 3 PbI 3. *Phys. Status Solidi RRL* **9,** 559–563; 10.1002/pssr.201510265 (2015).
8. Soufiani, A. M. *et al.* Polaronic exciton binding energy in iodide and bromide organic-inorganic lead halide perovskites. *Appl. Phys. Lett.* **107,** 231902; 10.1063/1.4936418 (2015).
9. Saba, M. *et al.* Correlated electron-hole plasma in organometal perovskites. *Nature communications* **5,** 5049; 10.1038/ncomms6049 (2014).
10. La-O-Vorakiat, C. *et al.* Elucidating the role of disorder and free-carrier recombination kinetics in CH3NH3PbI3 perovskite films. *Nature communications* **6,** 7903; 10.1038/ncomms8903 (2015).
11. Ledinsky, M. *et al.* Temperature Dependence of the Urbach Energy in Lead Iodide Perovskites. *The journal of physical chemistry letters* **10,** 1368–1373; 10.1021/acs.jpclett.9b00138 (2019).
12. Meggiolaro, D., Ambrosio, F., Mosconi, E., Mahata, A. & Angelis, F. de. Polarons in Metal Halide Perovskites. *Adv. Energy Mater.* **10,** 1902748; 10.1002/aenm.201902748 (2020).
13. Motta, C. *et al.* Revealing the role of organic cations in hybrid halide perovskite CH3NH3PbI3. *Nature communications* **6,** 7026; 10.1038/ncomms8026 (2015).

14. Herz, L. M. How Lattice Dynamics Moderate the Electronic Properties of Metal-Halide Perovskites. *The journal of physical chemistry letters* **9,** 6853–6863; 10.1021/acs.jpclett.8b02811 (2018).
15. heng, F. & Wang, L.-W. Large polaron formation and its effect on electron transport in hybrid perovskites. *Energy Environ. Sci.* **12,** 1219–1230; 10.1039/C8EE03369B (2019).
16. Ma, J. & Wang, L.-W. Nanoscale charge localization induced by random orientations of organic molecules in hybrid perovskite CH3NH3PbI3. *Nano letters* **15,** 248–253; 10.1021/nl503494y (2015).
17. Bonn, M., Miyata, K., Hendry, E. & Zhu, X.-Y. Role of Dielectric Drag in Polaron Mobility in Lead Halide Perovskites. *ACS Energy Lett.* **2,** 2555–2562; 10.1021/acsenergylett.7b00717 (2017).
18. Kang, B. & Biswas, K. Preferential CH 3 NH 3+ Alignment and Octahedral Tilting Affect Charge Localization in Cubic Phase CH 3 NH 3 PbI 3. *J. Phys. Chem. C* **121,** 8319–8326; 10.1021/acs.jpcc.7b01184 (2017).
19. Myung, C. W., Yun, J., Lee, G. & Kim, K. S. A New Perspective on the Role of A-Site Cations in Perovskite Solar Cells. *Adv. Energy Mater.* **8,** 1702898; 10.1002/aenm.201702898 (2018).
20. Ambrosio, F., Meggiolaro, D., Mosconi, E. & Angelis, F. de. Charge Localization, Stabilization, and Hopping in Lead Halide Perovskites: Competition between Polaron Stabilization and Cation Disorder. *ACS Energy Lett.* **4,** 2013–2020; 10.1021/acsenergylett.9b01353 (2019).
21. Nagai, M. *et al.* Longitudinal Optical Phonons Modified by Organic Molecular Cation Motions in Organic-Inorganic Hybrid Perovskites. *Physical review letters* **121,** 145506; 10.1103/PhysRevLett.121.145506 (2018).
22. Duan, H.-G. *et al.* Photoinduced Vibrations Drive Ultrafast Structural Distortion in Lead Halide Perovskite. *Journal of the American Chemical Society*; 10.1021/jacs.0c03970 (2020).
23. Munson, K. T., Kennehan, E. R., Doucette, G. S. & Asbury, J. B. Dynamic Disorder Dominates Delocalization, Transport, and Recombination in Halide Perovskites. *Chem* **4,** 2826–2843; 10.1016/j.chempr.2018.09.001 (2018).
24. K. Wang, M.C. Tang, H.X. Dang, R. Munir, D. Barrit, M. De Bastiani, E. Aydin, D.M. Smilgies, S. De Wolf, and A. Amassian, *Kinetic Stabilization of the Sol-Gel State in Perovskites Enables Facile Processing of High-Efficiency Solar Cells,* Adv. Mater. **31**, 1808357 (2019).
25. H. Dang, K. Wang, M.-C. Tang, M. De Bastiani, E. Aydin, E. Dauzon, D. Barrit, D.M. Smilgies, S. De Wolf, and A. Amassian, *Multi-Cation Synergy Suppresses Phase Segregation in Mixed-Halide Perovskites*, Joule **3**, 1746 (2019).
26. Ramakanth, S. & James Raju, K. C. Band gap narrowing in BaTiO 3 nanoparticles facilitated by multiple mechanisms. *Journal of Applied Physics* **115,** 173507; 10.1063/1.4871776 (2014).
27. Poglitsch, A. & Weber, D. Dynamic disorder in methylammoniumtrihalogenoplumbates (II) observed by millimeter-wave spectroscopy. *The Journal of Chemical Physics* **87,** 6373–6378; 10.1063/1.453467 (1987).
28. Mao, W. *et al.* Light-induced reversal of ion segregation in mixed-halide perovskites. *Nature materials* **20,** 55–61; 10.1038/s41563-020-00826-y (2021).
29. Elliott, R. J. Intensity of Optical Absorption by Excitons. *Phys. Rev.* **108,** 1384–1389; 10.1103/PhysRev.108.1384 (1957).
30. Amat, A. *et al.* Cation-induced band-gap tuning in organohalide perovskites: interplay of spin-orbit coupling and octahedra tilting. *Nano letters* **14,** 3608–3616; 10.1021/nl5012992 (2014).

31. Yang, Y. *et al.* Observation of a hot-phonon bottleneck in lead-iodide perovskites. *Nature Photon* **10,** 53–59; 10.1038/nphoton.2015.213 (2016).
32. Lim, J. W. M. *et al.* Hot Carriers in Halide Perovskites: How Hot Truly? *The journal of physical chemistry letters* **11,** 2743–2750; 10.1021/acs.jpclett.0c00504 (2020).
33. Li, M., Fu, J., Xu, Q. & Sum, T. C. Slow Hot-Carrier Cooling in Halide Perovskites: Prospects for Hot-Carrier Solar Cells. *Advanced materials (Deerfield Beach, Fla.)* **31,** e1802486; 10.1002/adma.201802486 (2019).
34. Schweizer, H. *et al.* Ionization of the Direct-Gap Exciton in Photoexcited Germanium. *Phys. Rev. Lett.* **51,** 698–701; 10.1103/PhysRevLett.51.698 (1983).
35. Aneesh, J. *et al.* Ultrafast Exciton Dynamics in Colloidal CsPbBr 3 Perovskite Nanocrystals: Biexciton Effect and Auger Recombination. *J. Phys. Chem. C* **121,** 4734–4739; 10.1021/acs.jpcc.7b00762 (2017).
36. Asano, K. & Yoshioka, T. Exciton–Mott Physics in Two-Dimensional Electron–Hole Systems: Phase Diagram and Single-Particle Spectra. *J. Phys. Soc. Jpn.* **83,** 84702; 10.7566/JPSJ.83.084702 (2014).
37. Jain, S. C. & Roulston, D. J. A simple expression for band gap narrowing (BGN) in heavily doped Si, Ge, GaAs and GexSi1−x strained layers. *Solid-State Electronics* **34,** 453–465; 10.1016/0038-1101(91)90149-S (1991).
38. Berggren, K.-F. & Sernelius, B. E. Band-gap narrowing in heavily doped many-valley semiconductors. *Phys. Rev. B* **24,** 1971–1986; 10.1103/PhysRevB.24.1971 (1981).
39. Lan, Y. *et al.* Ultrafast correlated charge and lattice motion in a hybrid metal halide perovskite. *Science advances* **5,** eaaw5558; 10.1126/sciadv.aaw5558 (2019).
40. Beni, G. & Rice, T. M. Theory of electron-hole liquid in semiconductors. *Phys. Rev. B* **18,** 768–785; 10.1103/PhysRevB.18.768 (1978).
41. Bretschneider, S. A. *et al.* Quantifying Polaron Formation and Charge Carrier Cooling in Lead-Iodide Perovskites. *Advanced materials (Deerfield Beach, Fla.),* e1707312; 10.1002/adma.201707312 (2018).
42. Juarez-Perez, E. J. *et al.* Photoinduced Giant Dielectric Constant in Lead Halide Perovskite Solar Cells. *The journal of physical chemistry letters* **5,** 2390–2394; 10.1021/jz5011169 (2014).
43. Wu, X. *et al.* Composition-Dependent Light-Induced Dipole Moment Change in Organometal Halide Perovskites. *J. Phys. Chem. C* **119,** 1253–1259; 10.1021/jp511314a (2015).
44. Almora, O., Aranda, C. & Garcia-Belmonte, G. Do Capacitance Measurements Reveal Light-Induced Bulk Dielectric Changes in Photovoltaic Perovskites? *J. Phys. Chem. C* **122,** 13450–13454; 10.1021/acs.jpcc.7b11703 (2018).
45. Nienhuys, H.-K. & Sundström, V. Intrinsic complications in the analysis of optical-pump, terahertz probe experiments. *Phys. Rev. B* **71,** 1759; 10.1103/PhysRevB.71.235110 (2005).
46. Karakus, M. *et al.* Phonon-Electron Scattering Limits Free Charge Mobility in Methylammonium Lead Iodide Perovskites. *The journal of physical chemistry letters* **6,** 4991–4996; 10.1021/acs.jpclett.5b02485 (2015).
47. Valverde-Chávez, D. A. *et al.* Intrinsic femtosecond charge generation dynamics in single crystal CH 3 NH 3 PbI 3. *Energy Environ. Sci.* **8,** 3700–3707; 10.1039/c5ee02503f (2015).
48. He, H. *et al.* Exciton localization in solution-processed organolead trihalide perovskites. *Nature communications* **7,** 10896; 10.1038/ncomms10896 (2016).

49. Thouin, F. *et al.* Phonon coherences reveal the polaronic character of excitons in two-dimensional lead halide perovskites. *Nature materials* **18,** 349–356; 10.1038/s41563-018-0262-7 (2019).
50. Langreth, D. C. & Kadanoff, L. P. Perturbation Theoretic Calculation of Polaron Mobility. *Phys. Rev.* **133,** A1070-A1075; 10.1103/PhysRev.133.A1070 (1964).
51. Wright, A. D. *et al.* Electron-phonon coupling in hybrid lead halide perovskites. *Nature communications* **7**; 10.1038/ncomms11755 (2016).
52. Frost, J. M., Whalley, L. D. & Walsh, A. Slow Cooling of Hot Polarons in Halide Perovskite Solar Cells. *ACS energy letters* **2,** 2647–2652; 10.1021/acsenergylett.7b00862 (2017).
53. Gao, Y. *et al.* Impact of Cesium/Rubidium Incorporation on the Photophysics of Multiple-Cation Lead Halide Perovskites. *Sol. RRL* **4,** 2000072; 10.1002/solr.202000072 (2020).

Supplementary Information

Ultrafast photo-enhancement of electron-phonon coupling in an organometal halide perovskite film

Mingcong Wang,[1,*] Yajun Gao,[1] Kai Wang,[1] Stefaan De Wolf,[1] Frédéric Laquai[1,*]

[1]King Abdullah University of Science and Technology (KAUST), KAUST Solar Center (KSC), Physical Sciences and Engineering Division (PSE), Material Science and Engineering Program (MSE), Thuwal 23955-6900, Kingdom of Saudi Arabia

Corresponding authors: mingcong.wang@kaust.edu.sa; frederic.laquai@kaust.edu.sa

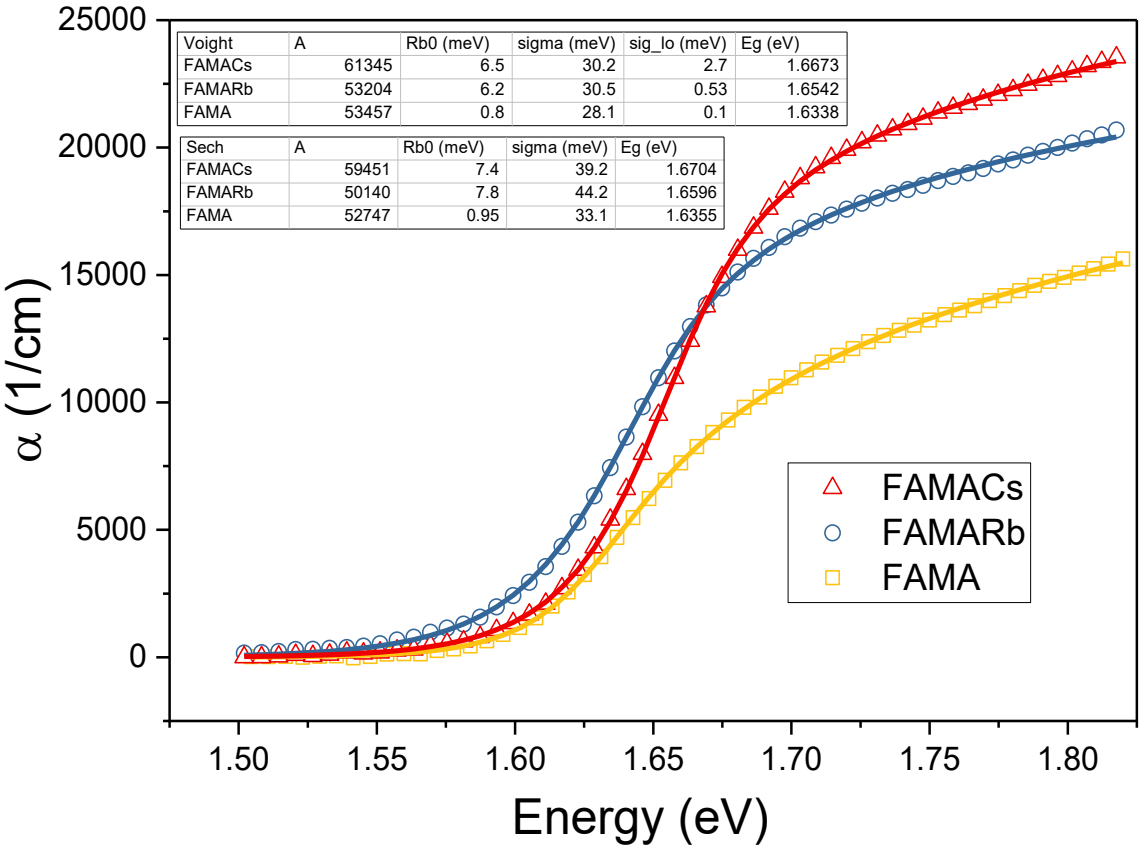

Figure S1: Elliott fitting to the ground-state absorption spectra. The inset tables list the fitting results obtained with two different broadening functions: Voight distribution and hyperbolic-secant distribution.

FAMACs: $Cs_{0.05}(FA_{0.83}MA_{0.17})_{0.95}Pb(I_{0.83}Br_{0.17})_3$

FAMARb: $Rb_{0.05}[(FA_{0.83}MA_{0.17})]_{0.95}Pb(I_{0.83}Br_{0.17})_3$

FAMA: $(FA_{0.83}MA_{0.17})Pb(I_{0.83}Br_{0.17})_3$

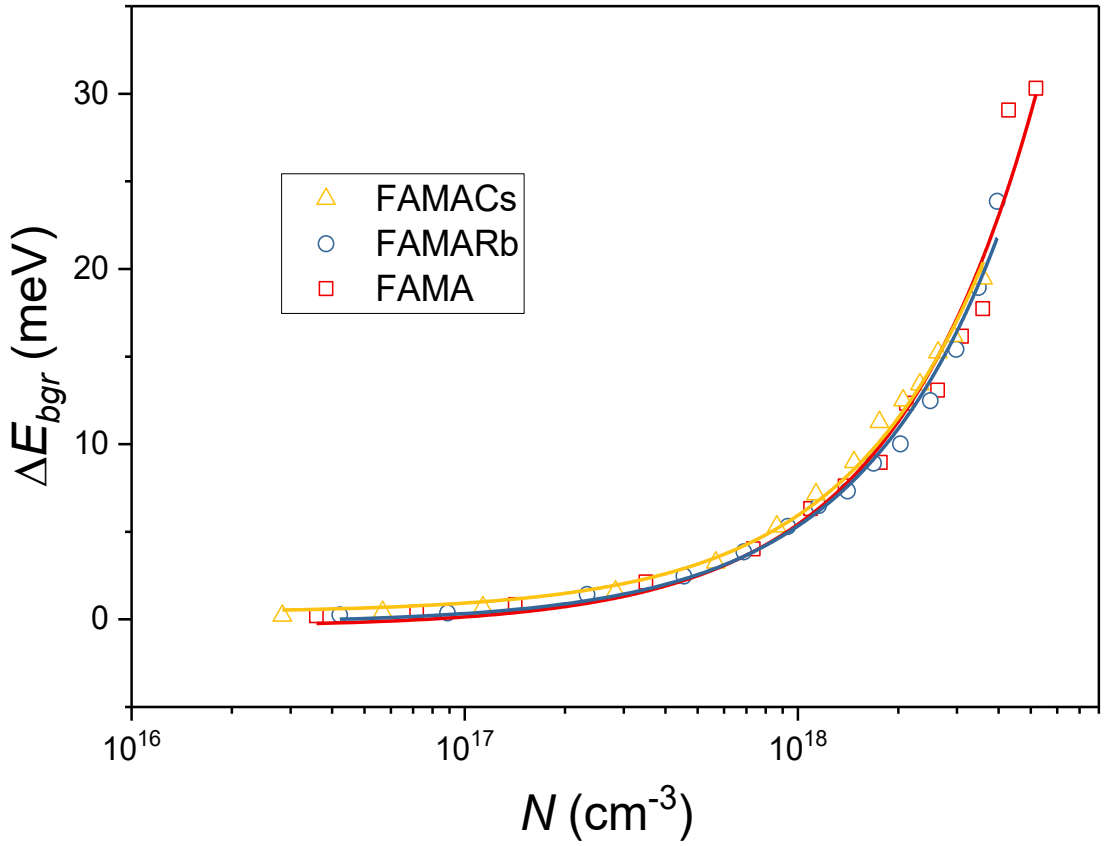

Figure S2: Photo-induced bandgap renormalization extracted from the high energy tails of the TA spectra for different perovskite films. Solid lines are linear fits to the data, respectively.

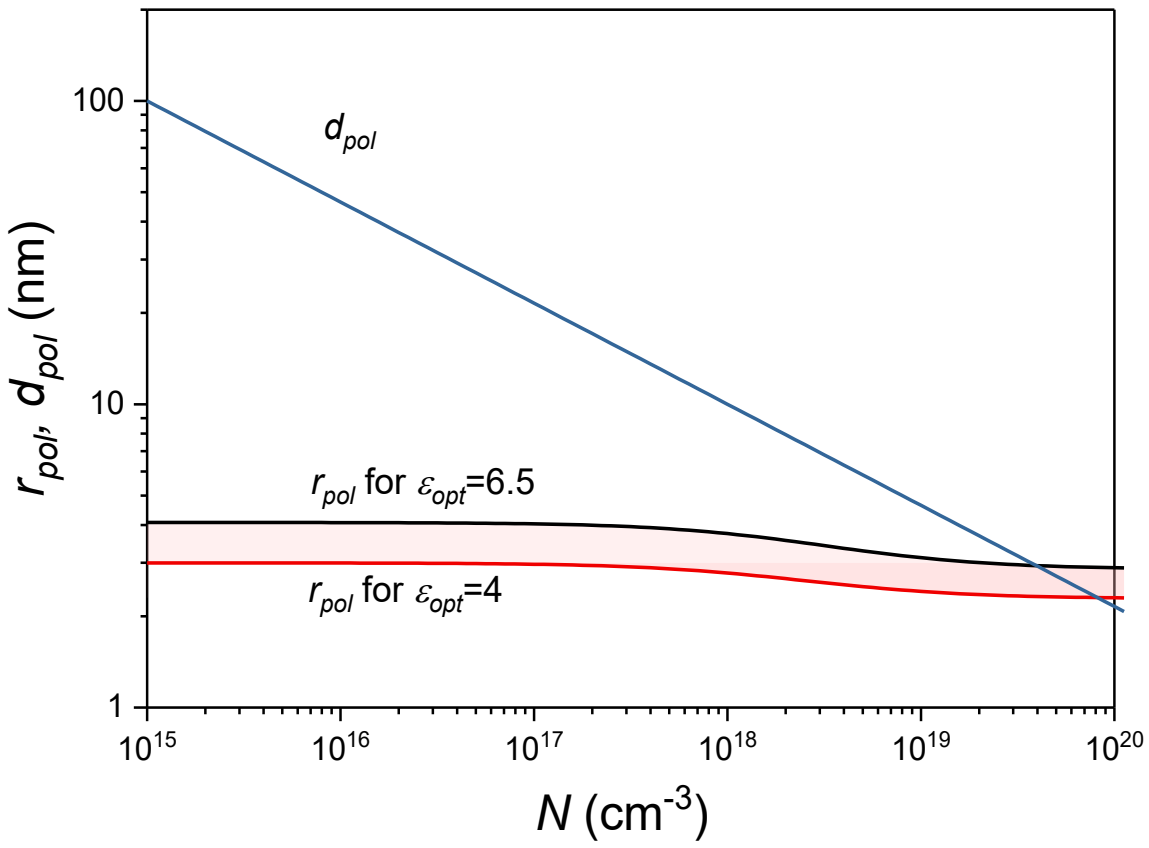

Figure S3: Polaron radius (r_{pol}) and the distance between two neighboring polars (d_{pol}) at different carrier densities, calculated using Eqn.13 in the main manuscript.

Section 1. Materials and sample preparation

Materials: PbI_2 and $PbBr_2$ were purchased from TCI. FAI and MABr were purchased from Dyesol. CsI, RbI and all anhydrous solvents (DMF, DMSO, chlorobenzene) were purchased from Sigma-Aldrich. SnO_2 colloid precursor was obtained from Alfa Aesar, the particles were diluted by H_2O and isopropanol to 2.67 %. All chemicals were used without further purification.

Perovskite film fabrication: PbI_2 (508 mg, 1.1 mmol), $PbBr_2$ (80.7 mg, 0.22 mmol), FAI (171.97 mg, 1 mmol) and MABr (22.4 mg, 0.2 mmol) in 1 mL of a 4: 1 (v/v) mixture of anhydrous DMF and DMSO. This resulting precursor solution for $(FA_{0.83}MA_{0.17})Pb(I_{0.83}Br_{0.17})_3$ contains a 10 mol% excess of PbI_2 and $PbBr_2$, respectively, which was introduced to enhance device performance. The FAMA solution was filtrated through a 0.45 μm syringe filter before use. CsI (389.7 mg, 1.5 mmol) was dissolved in 1 mL DMSO and 42 μL of the ~1.5 M CsI stock solution was added to 1 mL FAMA solution to get $Cs_{0.05}(FA_{0.83}MA_{0.17})_{0.95}Pb(I_{0.83}Br_{0.17})_3$ solution. RbI (318.5 mg, 1.5 mmol) was dissolved in 1 mL of DMSO and 42 μL of the ~1.5 M RbI stock solution was added to 1 mL FAMA solution to yield $Rb_{0.05}[(FA_{0.83}MA_{0.17})]_{0.95}Pb(I_{0.83}Br_{0.17})_3$ solution. For the solar cell performance please see Ref. 53 in the main article.

Section 2. Ground-state absorption coefficient

Ground-state absorption measurements were performed using a PerkinElmer Lambda 950 UV/Vis/NIR spectrophotometer. To reduce the impact of reflection on the absorption spectra, the absorption coefficient was calculated by:

$$\alpha(E) = -\frac{1}{d}\log\left(\frac{T}{1-R}\right) \qquad (S1)$$

where d is the sample thickness, R is the reflectivity, and T is the transmissivity.

Section 3. Transient absorption (TA) spectroscopy

Our TA setup uses a commercial Ti:sapphire amplifier operating at 800 nm with a repetition rate of 3 kHz as laser source. Its pulse width (FWHM) is compressed to ~125 fs. Two optical parametric amplifiers (OPA) are used to tune the laser wavelength. The white-light probe is generated by 1300 nm laser (from TOPAS1) with a CaF2 crystal that mounted on a continuously moving stage, which enables us to generate a super-continuum pulses with a spectral range from 350 to 1100 nm. The pump laser (from TOPAS2) is chopped to 1.5 KHz and delayed by an automated mechanical delay stage (Newport linear stage IMS600CCHA) from -400 ps to 8 ns. Pump and probe beams were overlapped on the front surface of the sample, and their spot sizes were measured by a beam viewer (Coherent, LaserCam-HR II) to make sure the pump beam was

about three times larger than the probe beam. The perovskite samples are stored in a nitrogen-filled chamber to protect from degradation, and photo-excited by 475 nm in this work. The probe beam was guided to a custom-made prism spectrograph (Entwicklungsbüro Stresing) where it was dispersed by a prism onto a 512 pixel complementary metal-oxide semiconductor (CMOS) linear image sensor (Hamamatsu G11608- 512DA). In order to account for the reflection, we first measured the transient reflection (R and $\Delta R/R$), then measured the transient absorption ($\Delta T/T$) and calculated the photo-induced change of absorption coefficient by:

$$\Delta\alpha(E) = \frac{1}{d}\log\left(\frac{T}{1-R}\right) - \frac{1}{d}\log\left(\frac{T'}{1-R'}\right) = \frac{1}{d}\log\left(\frac{1-\Delta T/T}{1-\frac{\Delta R/R}{1/R-1}}\right) \qquad (S2)$$

Section 4. Time-resolved terahertz spectroscopy setup (TRTS)

Our TRTS setup uses the same Ti:sapphire amplifier as the TA setup. The THz emitter and detector are two 1 mm thick <110> oriented zinc telluride (ZnTe) crystals. All the THz related optics were placed in a closed chamber, which was continuously purged with pure nitrogen gas. Perovskite samples were excited by 550 nm laser pulses obtained from the TOPAS2 in the TA setup. A rotation motor mounted with a circular ND filter was used to change the pump fluence in the fluence dependent experiments.

Section 5. Determination of the carrier density

The carrier densities injected by photoexcitation were calculated by:

$$N = F_{ph} \cdot \alpha\left(E_{pump}\right) \qquad (S3)$$

where F is the photon flux calculated by deducting the surface reflected photons from the total incident photons:

$$F_{ph} = \frac{P\left(1-R_{\mathrm{pump}}\right)}{1500 \cdot \pi \cdot (D_{\mathrm{FWHM}}/2)^2 \cdot E_{ph}}, \qquad E_{ph} = \frac{hc}{\lambda} \qquad (S4)$$

where P is the pump power. The number 1500 denotes the number of pulses that can pass the optical chopper in one second. D_{FWHM}~3.2 mm represents the full width at half maximum (FWHM) of the pump beam measured by the beam profiler.

The FWHM of the terahertz probe is calculated from the ratio of the maximum terahertz intensity transmitted through a 1-mm pinhole to its original intensity:

$$\mathrm{FWHM} = \sqrt{-\frac{\ln 2}{\ln(1-T_{max})}} \quad \mathrm{mm} \qquad (S5)$$

The diameter (FWHM) of the THz probe is ~1.13 mm as calculated from the measured T_{max} ~42%.

Section 6. Elliott fitting to the absorption spectra

The ground-state absorption spectra were fitted by the convolution of varies broadening functions (Eqn. S8) with the following Elliott formula:

$$\alpha(E) = A\frac{4\pi R_{b0}^{3/2}}{E}\delta(x + R_{b0}) + A\frac{\xi(R_{b0}, x)}{E}\sqrt{x} \tag{S6}$$

where

$$\xi(R_{b0}, x) = \frac{2\pi\sqrt{R_{b0}/x}}{1 - \exp\left(-2\pi\sqrt{R_{b0}/x}\right)}, \qquad x = E - E_g \tag{S7}$$

We tried three broadening function in the fitting: Gaussian, hyperbolic-secant and Voight (Gaussian convolute with Lorentzian). Both hyperbolic-secant distribution and Voight distribution can result in perfect fitting (Fig. S1). Since hyperbolic only have one parameter, we finally choose hyperbolic-secant distribution as the broadening function for simplicity.

$$Gaussian:\ G(E, \sigma) = \frac{1}{\sqrt{2\pi}\sigma}\exp\left(-\frac{E^2}{2\sigma^2}\right) \tag{S8a}$$

$$hyperbolicsecant:\ S(E, \sigma) = \frac{1}{2\sigma}\mathrm{sech}\left(-\frac{\pi E}{2\sigma}\right) \tag{S8b}$$

$$Voight:\ V(E, \sigma, \sigma_{lo}) = G(E, \sigma) \otimes \frac{\sigma_{lo}}{\pi}\frac{1}{E^2 + \sigma_{lo}^2} \tag{S8c}$$

The convolution of continuum absorption with an arbitrary broadening function is:

$$\frac{A}{E}\xi(R_{b0}, x)\sqrt{x} \otimes G(E, \sigma) = \frac{A}{E}\int_0^\infty \xi(R_{b0}, t)\sqrt{t}G(x - t, \sigma)dt \tag{S9}$$

When $x >> \sigma$, the broadening function is relatively sharp, we may consider $\xi(R_{b0}, t)t^{1/2}$ as slowly varying and take it out of the integration, then we have:

$$\frac{A}{E}\xi(R_{b0}, x)\sqrt{x} \otimes G(E, \sigma) \approx \frac{A}{E}\xi(R_{b0}, x)\sqrt{x} \tag{S10}$$

Then we can get the equation of photo-induced change of absorption shown in the main text (Eqn. 3).